

Spin-Orbital Locking, Emergent Pseudo-Spin, and Magnetic order in Na_2IrO_3

Subhro Bhattacharjee^{1,2}, Sung-Sik Lee^{2,3}, and Yong Baek Kim^{1,4}

¹ *Department of Physics, University of Toronto, Toronto, Ontario M5S 1A7, Canada.*

² *Department of Physics and Astronomy, McMaster University, Hamilton, Ontario L8S 4M1, Canada.*

³ *Perimeter Institute for Theoretical Physics, Waterloo, Ontario N2L 2Y5, Canada.*

⁴ *School of Physics, Korea Institute for Advanced Study, Seoul 130-722, Korea.*

(Dated: March 25, 2025)

The nature of magnetic order in the honeycomb lattice Iridate Na_2IrO_3 is explored by considering trigonal crystal field effect and spin-orbit coupling. An effective Hamiltonian is derived in terms of an emergent pseudo-spin-1/2, resulting from a spin-orbital locking, which is different from $j_{\text{eff}} = 1/2$ that is obtained when the spin-orbit coupling dominates. The resulting Hamiltonian is anisotropic and frustrated. Mean field theory suggests a ground state with 4-sublattice *zig-zag* magnetic order in the relevant parameter regime, in conformity with experiments. Various properties of the phase, the spin-wave spectrum and experimental consequences are discussed. This approach contrasts with the recent proposals of topological insulator or a Heisenberg-Kitaev system for this material, which fail to explain the observed magnetic properties.

PACS numbers: 71.70.Ej, 75.10.Dg, 75.10.Jm, 75.25.+z, 75.50.Ee

Interplay between strong spin-orbit (SO) coupling and electron-electron interaction in correlated electron systems has been a recent subject of intensive study [1–24]. In particular, 5*d* transition metal (e.g. Iridium or Osmium) oxides are regarded as ideal playgrounds for observing such cooperative effects [1–24]. Compared to 3*d* transition metal oxides, the Coulomb energy scale in these systems is reduced by the much larger extent of 5*d* orbitals while the SO coupling is enhanced due to high atomic number. Moreover, the system is very sensitive to the crystal fields owing to the extended 5*d* orbitals. As a result, the energy scales mentioned above often become comparable to each other, leading to a variety of competing phases. Precisely for this reason one expects to see possible emergent quantum phases in such systems. Indeed there have been several theoretical proposals for spin liquids, topological insulators and related phases in Iridium and Osmium oxides [10, 11, 14, 17, 19–22].

A notable example of such systems is Na_2IrO_3 , where Ir^{4+} ions form a honeycomb lattice. Taking into account the strong SO coupling in Ir^{4+} , proposed are a model for a topological insulator in the weak interaction limit [10] and a Heisenberg-Kitaev model for a possible spin liquid phase in the strong coupling limit [11]. These proposals prompted several experimental [4–6] and theoretical efforts [12] to understand the nature of the ground state in this material. However, it is found that Na_2IrO_3 orders magnetically at low temperatures [4]. The key experimental results are: (1) The magnetic transition occurs at $T_N = 15\text{K}$ while the Curie-Weiss temperature is about $\Theta_{CW} \approx -116\text{K}$. This indicates presence of frustration. (2) The high temperature magnetic susceptibility is anisotropic; the in-plane and out-of-plane susceptibilities are different. This may be due to a trigonal distortion of the IrO_6 octahedra [4]. (3) Recent resonant X-ray scattering experiment [5] suggests that the magnetic order is collinear and have a 4-site unit cell.

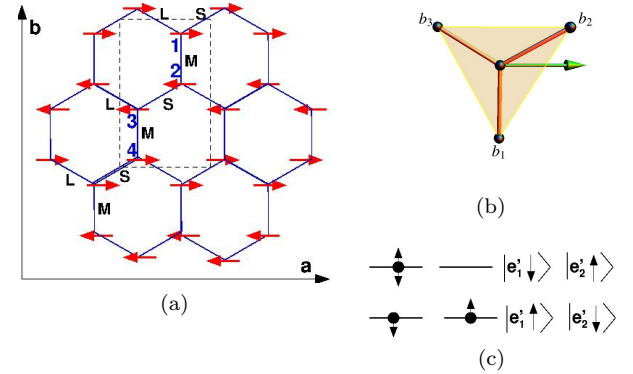


FIG. 1. (Colour Online) (a). The *zig-zag* magnetic structure as found in Ref. [5]. The unit cell has 4 sites. The modulation in the bond lengths are shown (L,S and M stands for long, short and medium bond-lengths respectively); (b) Section of a honeycomb lattice (shaded in yellow). Ir sites (black) are connected by bonds (orange). The green arrow is the the $[-1, -1, 1]$ direction of trigonal distortion that makes an angle of about 19° with the plane of the lattice pointing inside the plane; (c) The e'_g states split by the SO coupling.

(4) The magnetic moments have a large projection on the *a*-axis of the crystal. (5) Further they also find a modulation in the bond-lengths with the same periodicity as that of the magnetic structure. In combination of these experimental findings and density functional theory (DFT) calculations, it was strongly suggested that the ‘zig-zag’ pattern shown in Fig. 1(a) is the magnetic ground state. This magnetic order is not consistent with the ones that would be obtained by adding a weak interaction in a topological insulator (canted antiferromagnet) [10] or from a Heisenberg-Kitaev model (spin liquid or the so-called stripe antiferromagnet) [11].

In this letter, we propose a theory of the magnetic

order observed in Na_2IrO_3 . The effective Hamiltonian in the strong coupling limit is derived by taking into account both the crystal field effect due to a trigonal distortion of the oxygen octahedra around Ir^{4+} ions and SO coupling in the limit that the crystal field effect is larger than the SO coupling. In absence of the trigonal distortion and SO coupling, the cubic crystal field from the oxygen octahedra splits the atomic d -orbital levels to e_g and t_{2g} manifolds where the energy of the e_g levels is higher by about 3eV and can be ignored for five d -electrons in Ir^{4+} ions. The trigonal crystal field splits this t_{2g} manifold into e'_g (with two degenerate orbitals e'_{1g} and e'_{2g}) and non-degenerate a_{1g} . The e'_g and a_{1g} levels are occupied by three and two electrons in Ir^{4+} , respectively.

We show that, in the presence of SO coupling, the low energy degrees of freedom is described by an emergent pseudo-spin-1/2 doublet formed out of $|e'_{1g}, \downarrow\rangle$ and $|e'_{2g}, \uparrow\rangle$ states, where \uparrow and \downarrow represent the physical spin $s_z = 1/2, -1/2$ (the spins are quantized along the axis of trigonal distortion). Notice that the pseudo-spin results from (physical)spin-orbital *locking*, and the spin and orbital fluctuations are not separable. The resulting pseudo-spin-1/2 model in the strong coupling limit is given by Eq. 4 and corresponds to a Heisenberg model with an Ising anisotropy and further neighbour exchanges. A mean field treatment of this model yields a ground state with *zig-zag* magnetic order, as observed in the experiment. This solution also explain several other aspects of recent experiments as described below.

We emphasize that this is different from the much discussed splitting of the t_{2g} manifold to “effective total angular momentum” $j_{\text{eff}} = 1/2$ and $j_{\text{eff}} = 3/2$ multiplets in the strong SO coupling limit when trigonal crystal field is absent [2]. In this case, the low energy degrees of freedom is given by the half-filled $j_{\text{eff}} = 1/2$ level for Ir^{4+} . In fact, previous theories on a topological insulator and a Heisenberg-Kitaev model on Na_2IrO_3 are all based on this basis without the trigonal crystal field effect. However, when significant trigonal crystal field is present, as in Na_2IrO_3 [13], $j_{\text{eff}} = 1/2$ and $j_{\text{eff}} = 3/2$ are not well separated and they no longer serve as a useful basis.

Effective Hamiltonian: In the cubic environment the t_{2g} orbitals are degenerate when there is no SO coupling. In Na_2IrO_3 , there exists the trigonal distortion due to compression or expansion along one of the four C_3 axes of IrO_6 octahedra, which lifts this degeneracy. Although it is possible that the axes of trigonal distortions are different in different octahedra [20], we find that uniform distortions are more consistent with the experiments (see below). Let us denote the axis of this uniform trigonal distortion of the octahedron by the unit vector $\hat{n} = \frac{1}{\sqrt{3}}[n_1, n_2, n_3]$, where $n_\alpha = \pm 1$. Since there are 2 directions to each of the 4 trigonal axes we may choose a “gauge” to specify \hat{n} . This is done by taking $n_1 n_2 n_3 = +1$. The trigonal distortion splits the t_{2g} sector into the doubly degenerate e'_g and the non-degenerate

a_{1g} with energies $\Delta_{tri}/3$ and $-2\Delta_{tri}/3$ respectively. DFT results [13] suggest that $\Delta_{tri} \approx 600 \text{ meV}$. Hence the active orbitals are the 3/4-filled e'_g levels. The corresponding eigenstates are superposition of the t_{2g} orbitals [20].

A description based on Hubbard model for the e'_g orbitals may be systematically derived starting from the t_{2g} orbitals. This has the following general form

$$H' = - \sum_{ij} \sum_{M, M'} \sum_{\sigma} \tilde{t}_{iM; jM'} e_{iM\sigma}^\dagger e_{iM'\sigma} + \frac{U}{2} \sum_i \sum_{M, M'} \sum_{\sigma \sigma'} e_{iM\sigma}^\dagger e_{iM'\sigma'}^\dagger e_{iM'\sigma'} e_{iM\sigma}, \quad (1)$$

where $e_{iM\sigma}^\dagger$ is the electron creation operator in the e'_g orbital ($M = 1, 2$) with spin $\sigma (= \uparrow, \downarrow)$ and $\tilde{t}_{iM; jM'}$ are the effective hopping amplitudes within the subspace. We note that the Hund’s coupling (which arises from the orbital dependence of the Coulomb repulsion) for the t_{2g} orbitals only renormalizes U in this restricted subspace. (See supplement for details).

The SO coupling is included as follows. The angular momentum projected to the t_{2g} manifold acts as an effective orbital angular momentum $l_{\text{eff}} = 1$ with a negative SO coupling constant [2, 3, 15]. This, when further projected in the e'_g subspace, yields a block diagonal form:

$$H_{\text{SO}}^{e'_g} = -\lambda \hat{n} \cdot \vec{s}_i \tau_i^z, \quad (2)$$

where \vec{s}_i is the spin operator at the site i , $\lambda \approx 500 \text{ meV}$ is the SO coupling parameter and $\tau^z = +1(-1)$ refers to the e'_{1g} (e'_{2g}) orbital. Taking the direction of spin quantization same as the axis of trigonal distortion, we find that the active orbitals after including the SO coupling are the Krammer’s doublet $|e'_{1g}, \downarrow\rangle$ and $|e'_{2g}, \uparrow\rangle$ as shown in Fig. 1(c). On projecting to the subspace of $|e'_{1g}, \downarrow\rangle$ and $|e'_{2g}, \uparrow\rangle$, the spin and orbitals are no longer independent.

The bandwidth of this projected model is narrow and the effect of the Hubbard repulsion is important. Indeed it renders the system insulating. To capture the magnetic order in this Mott insulator, we do a strong-coupling expansion in \tilde{t}/U to get an effective “pseudo-spin” model in terms of the pseudo-spin-1/2 operators,

$$S^\alpha = \frac{1}{2} e_a^\dagger \rho_{ab}^\alpha e_b, \quad (3)$$

where, ρ^α ($\alpha = x, y, z$) are the Pauli matrices and $a, b = (e'_{g1}, \downarrow), (e'_{g2}, \uparrow)$. The “pseudo-spin” Hamiltonian has the following form up to the quadratic order:

$$H = \sum_{\langle ij \rangle} J_{ij}^{(1)} \vec{S}_i \cdot \vec{S}_j + \sum_{\langle\langle ij \rangle\rangle} J_{ij}^{(2)} \vec{S}_i \cdot \vec{S}_j + \sum_{\langle\langle\langle ij \rangle\rangle\rangle} J_{ij}^{(3)} \vec{S}_i \cdot \vec{S}_j + \sum_{\langle ij \rangle} J_{ij}^{(z1)} S_i^z S_j^z + \sum_{\langle\langle ij \rangle\rangle} J_{ij}^{(z2)} S_i^z S_j^z + \sum_{\langle\langle\langle ij \rangle\rangle\rangle} J_{ij}^{(z3)} S_i^z S_j^z. \quad (4)$$

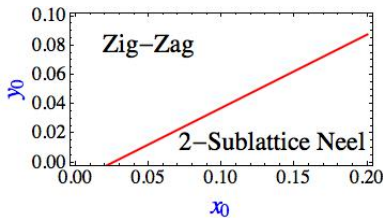


FIG. 2. (Colour Online) Mean field phase diagram for Eq. 4. The two axes are: $x_0 = \frac{J^{(01)}}{J^{(01)}}$; $y_0 = \frac{J^{(02)}}{J^{(01)}}$, where $J^{(01)}$ ($\tilde{J}^{(01)}$) are related to the strong(weak) NN exchange and $J^{(02)}$ is the 2^{nd} and 3^{rd} neighbour exchange (see Eq. 5). We take the Ising anisotropy to be 5% of $J^{(01)}$. DFT estimates give $x_0 \approx 0.1$, $y_0 \approx 0.065$ which falls in the zig-zag phase.

$$T_{ij}^{(0\alpha)} = \frac{1}{3} \left[(t_{ij}^{yz;yz} + t_{ij}^{xz;xz} + t_{ij}^{xy;xy}) - \frac{1}{2} (n_1 (t_{ij}^{xz;xy} + t_{ij}^{xy;xz}) + n_2 (t_{ij}^{xy;yz} + t_{ij}^{yz;xy}) + n_3 (t_{ij}^{yz;xz} + t_{ij}^{xz;yz})) \right] \quad (6)$$

$$T_{ij}^{(z\alpha)} = \frac{1}{2\sqrt{3}} [n_1 (t_{ij}^{xz;xy} - t_{ij}^{xy;xz}) + n_2 (t_{ij}^{xy;yz} - t_{ij}^{yz;xy}) + n_3 (t_{ij}^{yz;xz} - t_{ij}^{xz;yz})] \quad (7)$$

Clearly, the exchanges depend not only on the direction of the bond, but also the direction of the trigonal distortion. So it is important to ask about the direction of the latter. We note that the direction $[1, 1, 1]$ is perpendicular to the honeycomb plane while the other three directions make an acute angle to it. In the monoclinic $C2/C$ structure, uniform trigonal distortion in these four directions may not cost the same energy. In experiments [5], the moments are seen to point along the a -axis of the monoclinic crystal which is parallel to the honeycomb plane. This, along with the fact that the magnetic moment in our model is in the direction of \hat{n} (explained below) seems to suggest that $\hat{n} = \frac{1}{\sqrt{3}}[-1, -1, 1]$ is chosen in the compound. In the absence of a better theoretical understanding of the direction of the trigonal distortion, we take this as an input from the experiments. Our assumption seems to be in conformity with the modulation in the bond-lengths (see Fig. 1(a) and discussions below).

To identify different hopping paths (both direct and indirect), we use the results of the DFT analysis and corresponding tight binding parameters by Jin *et al.* [13, 25]. Considering the various exchange paths (see supplement) we find, while $J^{(3z)} = 0$, $J^{(1z)} \neq J^{(2z)} \neq 0$ are approximately (spatially-)isotropic and antiferromagnetic. For the exchanges of the Heisenberg terms, we find both $J^{(2)}$ and $J^{(3)}$ are antiferromagnetic and isotropic (and approximately equal according to the tight-binding fit of the DFT results [13, 25]). For the NN Heisenberg exchanges, the couplings are much more spatially anisotropic. We find that for the chosen direction of the trigonal distortion, the coupling along one of the NN exchanges (*viz* b_1 in Fig. 1(b)) may be large and antiferromagnetic, while for the other two neighbours (b_2 and b_3 in Fig. 1(b)), it

Here $\langle ij \rangle$, $\langle\langle ij \rangle\rangle$ and $\langle\langle\langle ij \rangle\rangle\rangle$ refer to summation over first, second and third nearest neighbours (NNs) respectively.

The different exchange couplings are given in terms of the underlying parameters of the Hubbard model as

$$J_{ij}^{(z\alpha)} = \frac{8}{U} (T_{ij}^{(z\alpha)})^2, \\ J_{ij}^{(\alpha)} = \frac{4}{U} [(T_{ij}^{(0\alpha)})^2 - (T_{ij}^{(z\alpha)})^2] = J_{ij}^{(0\alpha)} - \frac{1}{2} J_{ij}^{(z\alpha)} \quad (5)$$

where $\alpha = 1, 2, 3$ denotes that ij are first, second or third NNs, respectively and the last expression defines $J_{ij}^{(0\alpha)}$. $T_{ij}^{(0\alpha)}$ and $T_{ij}^{(z\alpha)}$ are given in terms of the hopping amplitudes (e.g. $t_{ij}^{xy;yz}$ from the overlap of xy and yz orbitals) of the t_{2g} orbitals as

is weakly antiferromagnetic (comparable with $J^{(2)}$, $J^{(3)}$).

Mean-Field Theory and Magnetic Order: The classical ground state for the model can be calculated within mean-field theory and shows a region of the parameter-space where the zig-zag order is stabilized. The parameters calculated from DFT falls within this regime. The effect of the Ising anisotropies $J^{(1z)}$ and $J^{(2z)}$ is to pin the magnetic ordering along the z -direction of the pseudo-spin quantization which is also the direction of the trigonal distortion \hat{n} . They also gap out any Goldstone mode that arises from the ordering of the pseudo-spins. This may be the origin of the suppression of the specific heat with lowering temperature. The other competing phase with a collinear order is the regular two-sublattice Neel Phase. A mean-field phase diagram is shown in Fig. 2.

The nature of the ground states may be understood from the following arguments. In the presence of the \hat{n} in $[-1, -1, 1]$ direction, the NN exchange coupling becomes anisotropic. While it is strong in one direction, it is weak in two other directions. For the bonds where the NN coupling becomes weak, the effects of the small second and third neighbour interactions become significant. Since the latter interactions are antiferromagnetic, they prefer anti-parallel alignment of the spins. Since there are more second and third neighbours, their cumulative effect can be much stronger. This naturally leads to the zig-zag state. The NN antiferromagnetic interactions on the weaker bonds compete with the antiferromagnetic second and third neighbour interactions and frustrates the magnet. This explains why the magnetic ordering occurs far below the Curie-Weiss temperature.

Further Experimental Implications: The relation between the magnetic moment and the pseudo-spins is

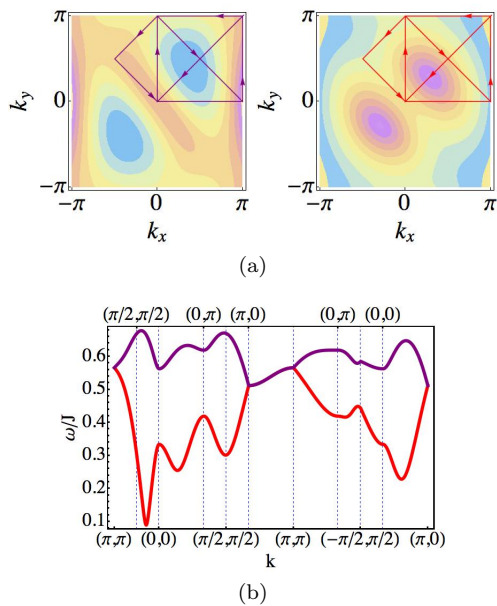


FIG. 3. (Colour Online) The “pseudo-spin” wave spectrum (contours of both the bands are shown in (a) and a section is shown in (b)). The values used for the parameters are same as that used for the calculation of the mean field phase diagram (Fig. 2). We note that, as expected, the spectrum is gapped.

given by

$$\vec{M}_i = -4\mu_B \hat{n} S_i^z, \quad (8)$$

where μ_B is the Bohr magneton. This follows from the twin facts that, in e'_g subspace, the angular momentum transverse to \hat{n} is quenched and the spins are locked to the orbitals with the axis of quantization being \hat{n} in our pseudo-spin sector (see supplement). Thus, the magnetization is sensitive to the z -component of the pseudo-spin (the direction of which is shown in Fig. 1(a)). Indeed the magnetization has the largest projection along the a -axis of the monoclinic crystal. This was seen in experiments [5] and was indeed the motivation for choosing the $[-1, -1, 1]$ direction for the trigonal distortion. Along two other axes $[-1, 1, -1]$ and $[1, -1, -1]$, a large component of in-plane magnetization exists, but in different directions. Finally the direction $[1, 1, 1]$ is perpendicular to the honeycomb plane and leads to magnetization in the same $[1, 1, 1]$ direction. While this does not appear to be the case for Na_2IrO_3 , this may be more relevant for the less-distorted compound Li_2IrO_3 (see below).

Eq. 8 suggests that the magnetic susceptibility is highly anisotropic and depends on the cosine of the angle between the direction of magnetic field and \hat{n} . Indeed signatures of such anisotropy have been already seen in experiments [4]. We emphasize that within this picture, the in-plane susceptibility also varies with the direction of the magnetic field. However, this picture is strictly based on atomic orbitals. One generally expects that there is also hybridization of the Ir d -orbitals with the

oxygen p -orbitals. Such hybridization will contribute to a non-zero isotropic component to the susceptibility [24].

A representative spin wave spectrum in the zig-zag phase is shown in Fig. 3(a) and 3(b). The spectrum is gapped and the bottom of the spin-wave dispersion has some characteristic momentum dependence. Signatures of such excitations may be seen in future resonant X-Ray scattering experiments. It is important to note that this “pseudo-spin” waves actually contain both orbital and the spin components due to the spin-orbital locking.

Summary and Conclusion: Here we have studied the effect of trigonal distortion and SO coupling for the honeycomb lattice compound Na_2IrO_3 . We have explained the magnetic order, calculated the low energy spin-wave spectrum and elucidated various properties of the compound that has been observed in experiment. In these lights, it is tempting to predict the case of Li_2IrO_3 where recent experiments suggest a more isotropic honeycomb lattice. This may be due to the axis of trigonal distortion being perpendicular to the plane. What may be the fallouts in such a case? Our present analysis would suggest that the antiferromagnet exchanges are isotropic and equally strong for the three NNs. This would develop 2-sublattice Neel order in the pseudo-spins with the magnetic moments being perpendicular to the plane. Also the further neighbour exchanges are rather weak and hence frustration is quite small. Indeed recent experiments see ordering very close to the Curie-Weiss temperature, the later being calculated from the high temperature magnetic susceptibility data [6, 26].

We acknowledge useful discussion with H. Gretarsson, R. Comin, S. Furukawa, H. Jin, C. H. Kim, Y.-J. Kim, W. Witzak-Krempa, H. Takagi. YBK thanks the Aspen Center for Physics, where parts of the research were done.

-
- [1] Y. Okamoto, M. Nohara, H. Aruga-Katori, and H. Takagi, Phys. Rev. Lett.99, 137207 (2007).
 - [2] B. J. Kim *et al.*, Phys. Rev. Lett.101, 076402 (2008)
 - [3] B. J. Kim *et al.*, Science 323, 1329 (2009).
 - [4] Y. Singh and P. Gegenwart, Phys. Rev. B82, 064412 (2010).
 - [5] X. Liu, T. Berlijn, W.-G. Yin, W. Ku, A. Tsvelik, Y.-J. Kim, H. Gretarsson, Y. Singh, P. Gegenwart, and J. P. Hill, arXiv:1104.4046.
 - [6] Y. Singh, S. Manni, and P. Gegenwart, arXiv:1106.0429.
 - [7] S. Nakatsuji *et al.*, Phys. Rev. Lett.96, 087204 (2006).
 - [8] S. Zhao, J. M. Mackie, D. E. MacLaughlin, O. O. Bernal, J. J. Ishikawa, Y. Ohta, and S. Nakatsuji, arXiv:1104.1213.
 - [9] F. F. Tafti, J. J. Ishikawa, A. McCollam, S. Nakatsuji, and S. R. Julian, arXiv:1107.2544.
 - [10] A. Shitade *et al.*, Phys. Rev. Lett.102, 256403 (2009).
 - [11] J. Chaloupka, G. Jackeli, and G. Khaliullin, Phys. Rev. Lett.105, 027204 (2010); G. Jackeli and G. Khaliullin, Phys. Rev. Lett.102, 017205 (2009).
 - [12] H.-C. Jiang, Z.-C. Gu, X.-L. Qi, and S. Trebst, Phys.

- Rev. B 83, 245104 (2011).
- [13] H. Jin *et al.*, arXiv:0907.0743.
 - [14] M. J. Lawler, A. Paramekanti, Y. B. Kim, and L. Balents, Phys. Rev. Lett.101, 197202 (2008).
 - [15] G. Chen and L. Balents, Phys. Rev. B78, 094403 (2008).
 - [16] M. R. Norman and T. Micklitz, Phys. Rev. Lett.102, 067204 (2009).
 - [17] D. Podolsky, A. Paramekanti, Y. B. Kim, T. Senthil, Phys. Rev. Lett.102, 186401 (2009).
 - [18] D. Podolsky, Y. B. Kim, Phys. Rev. B83, 054401 (2011).
 - [19] D. Pesin and L. Balents, Nat Phys 6, 376 (2010)
 - [20] B.-J. Yang and Y. B. Kim, Phys. Rev. B82, 085111 (2010).
 - [21] X. Wan, A. Turner, A. Vishwanath, S. Y. Savrasov, Phys. Rev. B83, 205101 (2011); X. Wan, A. Vishwanath, S. Y. Savrasov, arXiv:1103.4634.
 - [22] W. Witczak-Krempa, Y. B. Kim, arXiv:1105.6108.
 - [23] F. Wang, and T. Senthil, Phys. Rev. Lett.106, 136402 (2011).
 - [24] G. Chen, R. Pereira, and L. Balents, arXiv:1009.5115.
 - [25] H. Jin, C. H. Kim (Private communication).
 - [26] H. Takagi (Private Communication).

SUPPLEMENTARY MATERIAL

The Trigonal Hamiltonian

The Hamiltonian for trigonal distortion, when projected in the t_{2g} sector, gives [20] (in our chosen *gauge*)

$$H_{tri}^{t_{2g}} = \sum_i \frac{-\Delta_{tri}}{3} \Psi_i^\dagger \begin{bmatrix} 0 & n_3 & n_2 \\ n_3 & 0 & n_1 \\ n_2 & n_1 & 0 \end{bmatrix} \Psi_i, \quad (9)$$

where $\Psi_i^\dagger = [d_{yz}^\dagger, d_{zx}^\dagger, d_{xy}^\dagger]$ and Δ_{tri} is the energy scale for trigonal distortion. The eigenstates are ($\omega = e^{i2\pi/3}$)

$$\begin{aligned} E_{a_{1g}} &= -\frac{2\Delta_{tri}}{3}; & |a_{1g}\rangle &= \frac{1}{\sqrt{3}} [n_1|d_{yz}\rangle + n_2|d_{zx}\rangle + n_3|d_{xy}\rangle], \\ E_{e'_{1g}} &= \frac{\Delta_{tri}}{3}; & |e'_{1g}\rangle &= \frac{1}{\sqrt{3}} [\omega n_1|d_{yz}\rangle + \omega^2 n_2|d_{zx}\rangle + n_3|d_{xy}\rangle], \\ E_{e'_{2g}} &= \frac{\Delta_{tri}}{3}; & |e'_{2g}\rangle &= \frac{1}{\sqrt{3}} [\omega^2 n_1|d_{yz}\rangle + \omega n_2|d_{zx}\rangle + n_3|d_{xy}\rangle], \end{aligned} \quad (10)$$

The microscopic model for Na_2IrO_3

The generic Hubbard model (for the t_{2g} orbitals) including the trigonal distortions and the SO coupling is

$$H = -\lambda \sum_i \vec{l}_i \cdot \vec{s}_i + H_{tri}^{t_{2g}} + \sum_{ij} \sum_{mm'} \sum_{\sigma\sigma'} \left(t_{ij}^{m;m'} d_{im\sigma}^\dagger d_{jm'\sigma'} \right) + \frac{1}{2} \sum_i \sum_{mm'} \sum_{\sigma\sigma'} U_{mm'} d_{im\sigma}^\dagger d_{im'\sigma'}^\dagger d_{im'\sigma'} d_{im\sigma}. \quad (11)$$

Here $m, m' = yz, xz, xy$ and $\sigma = \uparrow, \downarrow$. We note that the hopping is diagonal in spin space and in the cubic harmonic basis all hopping are real. Also, the hopping contain both the direct and indirect (through Oxygen and Sodium) paths. We have taken Hund's coupling into account through $U_{mm'}$, though this is expected to be small in $5d$ transition metals. To a very good approximation the form of $U_{mm'}$ is given by

$$U_{mm'} \equiv \begin{bmatrix} U_0 & U_0 - J_H & U_0 - J_H \\ U_0 - J_H & U_0 & U_0 - J_H \\ U_0 - J_H & U_0 - J_H & U_0 \end{bmatrix}, \quad (12)$$

where the basis is given, as before, by $\Psi_i^\dagger = [d_{yz}^\dagger, d_{zx}^\dagger, d_{xy}^\dagger]$. U_0 and J_H are the intra orbital Coulomb repulsion and Hund's coupling term respectively.

The transformation between the operators in the trigonal basis, $\Phi^\dagger = [a_{1g}^\dagger, e'_{1g}^\dagger, e'_{2g}^\dagger]$, and t_{2g} basis, $\Psi^\dagger = [d_{yz}^\dagger, d_{zx}^\dagger, d_{xy}^\dagger]$, is given by $\Psi_m = T_{m,M} \Phi_M$. The transformation matrix is given by

$$T_{m,M} = \frac{1}{\sqrt{3}} \begin{bmatrix} n_1 & n_1\omega & n_1\omega^2 \\ n_2 & n_2\omega^2 & n_2\omega \\ n_3 & n_3 & n_3 \end{bmatrix}. \quad (13)$$

The transformations for the hopping amplitudes and repulsion term are then given by

$$\tilde{t}_{iM;jM'} = \sum_{m,m'} T_{m,M}^* t_{ij}^{m;m'} T_{m',M'}; \quad \tilde{U}_{M_1 M_2} = \sum_{m,m'} U_{mm'} (T_{mM_1}^* T_{mM_1}) (T_{m'M_2}^* T_{m'M_2}); \quad (14)$$

As shown below, the different contributions to $t_{ij}^{m;m'}$ are obtained from the fitting of the DFT calculations by H. Jin *et al.* [13]. These show that there are contributions from both direct and indirect hoppings for the first, second and third nearest neighbours. Projecting them into the e'_g orbitals we get the effective hopping amplitudes which are then used in Eq. 1. As for the Coulomb repulsion term, we find that it has the following form

$$\tilde{U}_{M_1 M_2} = U \begin{bmatrix} 1 & 1 & 1 \\ 1 & 1 & 1 \\ 1 & 1 & 1 \end{bmatrix}, \quad (15)$$

where $U = U_0 - 2J_H/3$. This form is then used in Eq. 1. The reason for this special form of $\tilde{U}_{M_1 M_2}$ lies in the fact that the e'_g orbitals have equal weight of the three t_{2g} orbitals (see the wave functions above).

Projection of Spin-Orbit coupling to the e'_g subspace

The SO coupling, when projected to the t_{2g} orbitals give

$$H_{\text{SO}}^{t_{2g}} = -\lambda \vec{l} \cdot \vec{s}, \quad (16)$$

where \vec{l} is a $l = 1$ angular momentum operator. We can re-write the t_{2g} cubic harmonics in terms of the spherical harmonics of the effective $l = 1$ angular momentum operator. These are given by:

$$|d_{yz}\rangle = \frac{1}{\sqrt{2}} [|1, -1\rangle - |1, +1\rangle]; \quad |d_{zx}\rangle = \frac{i}{\sqrt{2}} [|1, -1\rangle + |1, -1\rangle]; \quad |d_{xy}\rangle = |1, 0\rangle \quad (17)$$

The projector for the e'_g space is: $P^{e'_g} = |e'_1\rangle\langle e'_1| + |e'_2\rangle\langle e'_2|$. It turns out that $\vec{l} \cdot \vec{s}$ is block diagonal in this subspace. Hence

$$\vec{l} \cdot \vec{s} = |e'_1\rangle\langle e'_1| \vec{l} \cdot \vec{s} |e'_1\rangle\langle e'_1| + |e'_2\rangle\langle e'_2| \vec{l} \cdot \vec{s} |e'_2\rangle\langle e'_2| \quad (18)$$

Making the ‘‘gauge’’ choice we get

$$\langle e'_1 | \vec{l} \cdot \vec{s} | e'_1 \rangle = \hat{n} \cdot \vec{s}; \quad \langle e'_2 | \vec{l} \cdot \vec{s} | e'_2 \rangle = -\hat{n} \cdot \vec{s} \quad (19)$$

Projection of Zeeman term in the t_{2g} and $\{|e'_{1g} \downarrow\rangle, |e'_{2g} \uparrow\rangle\}$ subspaces.

The Zeeman coupling term, when projected to the t_{2g} space, gives

$$H_Z^{t_{2g}} = \mu_B \left(-\vec{l} + 2\vec{s} \right) \cdot \vec{B}. \quad (20)$$

Thus the magnetization after projection is given by:

$$\vec{M}^{t_{2g}} = \mu_B \left(-\vec{l} + 2\vec{s} \right) \quad (21)$$

This when projected to the subspace $|e'_1, \uparrow\rangle$ and $|e'_2, \downarrow\rangle$ gives (using the Block diagonal property of the orbital angular momentum as above):

$$\tilde{H}_Z = 4\mu_B S^z \hat{n} \cdot \vec{B} \quad (22)$$

where \vec{S} (note that this is in upper case compared to the physical spin written lower case) is the emergent pseudo-spin-1/2 per site. This pseudo-spin is generated by the operators Eq. 3. This is the emergent degree of freedom at low energies. Clearly, the magnetic moment is then given by Eq. 8.

The hopping parameters

Nearest neighbours

The nearest neighbours are shown in Fig. 4(a). There are two different processes contributing to the hopping.: 1) the direct hopping between the Ir atoms and 2) the indirect hopping between the Ir atoms mediated by the oxygen atoms. In presence of the trigonal distortion which has a component along the honeycomb plane (like in this case $[-1, -1, 1]$) the magnitudes of the different hopping parameters are different in different directions (for both direct and indirect hopping). The results are shown in Table I.

We shall make an approximation here. We shall leave out the directional dependence of the magnitudes on the direction. The argument is that the essential directional dependence due to the trigonal distortion has been taken care of by the parameter Δ_1 . The DFT results have been used to find the tight-binding parameters. They use $\Delta_1 = 0$ and find (here t_{dd1} and t_{dd2} are direct hopping and t_0 is the indirect hopping respectively.) $t_{dd1} = -0.5 \text{ eV}; t_{dd2} = 0.15 \text{ eV}; t_0 = 0.25 \text{ eV}$.

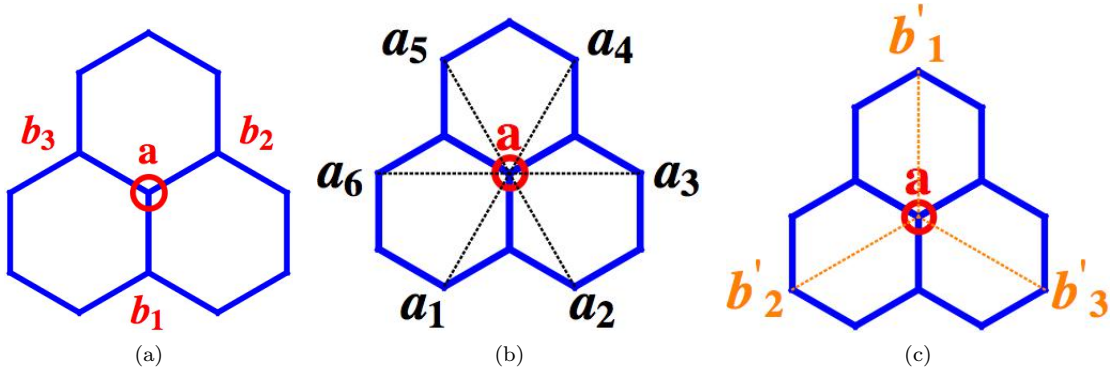


FIG. 4. (Colour Online) The 3 nearest neighbours (a), six 2^{nd} nearest neighbours (b) and three 3^{rd} nearest neighbours (c) of the central site. The nomenclature has been used to label the hoppings.

(a)NN: $t_{am};b_1m'$

$m' \setminus m$	d_{xy}	d_{yz}	d_{zx}
d_{xy}	$t_{dd1}(b_1)$	-	-
d_{yz}	-	$t_{dd2}(b_1)$	$-t_{dd2}(b_1) + t_0(b_1) + \Delta_1(b_1)$
d_{zx}	-	$-t_{dd2}(b_1) + t_0(b_1) - \Delta_1(b_1)$	$t_{dd2}(b_1)$

(b)NN: $t_{am};b_2m'$

$m' \setminus m$	d_{xy}	d_{yz}	d_{zx}
d_{xy}	$t_{dd2}(b_2)$	-	$-t_{dd2}(b_2) + t_0(b_2) + \Delta_1(b_2)$
d_{yz}	-	$t_{dd1}(b_2)$	-
d_{zx}	$-t_{dd2}(b_2) + t_0(b_2) - \Delta_1(b_2)$	-	$t_{dd2}(b_2)$

(c)NN: $t_{am};b_3m'$

$m' \setminus m$	d_{xy}	d_{yz}	d_{zx}
d_{xy}	$t_{dd2}(b_3)$	$-t_{dd2}(b_3) + t_0(b_3) + \Delta_1(b_3)$	-
d_{yz}	$-t_{dd2}(b_3) + t_0(b_3) - \Delta_1(b_3)$	$t_{dd2}(b_3)$	-
d_{zx}	-	-	$t_{dd1}(b_3)$

TABLE I. The hopping paths (both direct and indirect) in the t_{2g} basis.

Performing the transformation to the e'_g basis, we have

$$T_{ab_1}^{(01)} = \frac{1}{3} [t_{dd1} + 2t_{dd2} + (t_{dd2} - t_0)n_3], \quad T_{ab_1}^{(z1)} = -\frac{\Delta_1}{\sqrt{3}}n_3 \quad (23)$$

$$T_{ab_2}^{(02)} = \frac{1}{3} [t_{dd1} + 2t_{dd2} + (t_{dd2} - t_0)n_1], \quad T_{ab_2}^{(z1)} = -\frac{\Delta_1}{\sqrt{3}}n_1 \quad (24)$$

$$T_{ab_3}^{(03)} = \frac{1}{3} [t_{dd1} + 2t_{dd2} + (t_{dd2} - t_0)n_2], \quad T_{ab_3}^{(z1)} = -\frac{\Delta_1}{\sqrt{3}}n_2 \quad (25)$$

Hence,

$$J_{ab_1}^{(0)} = \frac{4}{3U} \left[\frac{1}{3} [t_{dd1} + 2t_{dd2} + (t_{dd2} - t_0)n_3]^2 - (\Delta_1)^2 \right], \quad J_{ab_1}^{(1z)} = \frac{8(\Delta_1)^2}{3U}; \quad (26)$$

$$J_{ab_2}^{(0)} = \frac{4}{3U} \left[\frac{1}{3} [t_{dd1} + 2t_{dd2} + (t_{dd2} - t_0)n_1]^2 - (\Delta_1)^2 \right], \quad J_{ab_2}^{(1z)} = \frac{8(\Delta_1)^2}{3U}; \quad (27)$$

$$J_{ab_3}^{(0)} = \frac{4}{3U} \left[\frac{1}{3} [t_{dd1} + 2t_{dd2} + (t_{dd2} - t_0)n_2]^2 - (\Delta_1)^2 \right], \quad J_{ab_3}^{(1z)} = \frac{8(\Delta_1)^2}{3U}; \quad (28)$$

where we have taken the direction of the trigonal distortion is taken to be uniform.

Second nearest neighbour

These are shown in Fig. 4(b). These indirect hoppings are mediated by the Na atoms. In general, in presence of the trigonal distortion in the $[-1, -1, 1]$ direction, the magnitude of the hopping amplitudes are also direction dependent. However, since the magnitudes themselves are expected to be small we shall neglect such directional dependence in the magnitudes. The result is summarized in Table II.

(a)NNN: $t_{am;a_1m'}/t_{am;a_4m'}$				(b)NNN: $t_{am;a_2m'}/t_{am;a_5m'}$				(c)NNN: $t_{am;a_3m'}/t_{am;a_6m'}$			
$m' \setminus m$	d_{xy}	d_{yz}	d_{zx}	$m' \setminus m$	d_{xy}	d_{yz}	d_{zx}	$m' \setminus m$	d_{xy}	d_{yz}	d_{zx}
d_{xy}	-	$t_2 + \Delta_2$	-	d_{xy}	-	-	$t_2 + \Delta_2$	d_{xy}	-	-	-
d_{yz}	$t_2 - \Delta_2$	-	-	d_{yz}	-	-	-	d_{yz}	-	-	$t_2 + \Delta_2$
d_{zx}	-	-	-	d_{zx}	$t_2 - \Delta_2$	-	-	d_{zx}	-	$t_2 - \Delta_2$	-

TABLE II. Hopping paths for the second nearest neighbours

So for the e'_g basis, we have

$$\begin{aligned}
 T_{a,a_1}^{(02)} = T_{a,a_4}^{(02)} &= -\frac{t_2}{3}n_2, & T_{a,a_1}^{(z2)} = T_{a,a_4}^{(z2)} &= -\frac{\Delta_2}{\sqrt{3}}n_2 \\
 T_{a,a_2}^{(02)} = T_{a,a_5}^{(02)} &= -\frac{t_2}{3}n_1, & T_{a,a_2}^{(z2)} = T_{a,a_5}^{(z2)} &= -\frac{\Delta_2}{\sqrt{3}}n_1 \\
 T_{a,a_3}^{(02)} = T_{a,a_6}^{(02)} &= -\frac{t_2}{3}n_3, & T_{a,a_3}^{(z2)} = T_{a,a_6}^{(z2)} &= -\frac{\Delta_2}{\sqrt{3}}n_3
 \end{aligned} \tag{29}$$

Tight binding fit of the DFT data uses only t_2 and finds $t_2 \approx -0.075$ eV. Therefore we have:

$$J_{a,a_\alpha}^{(2)} = \frac{4}{3U} \left[\frac{(t_2)^2}{3} - (\Delta_2)^2 \right], \quad J_{a,a_\alpha}^{(2z)} = \frac{8(\Delta_2)^2}{3U}. \tag{30}$$

Third nearest neighbour

The third nearest neighbours are listed in Fig. 4(c). The hopping to the third nearest neighbour is mediated by the Na atoms. Again we shall neglect the directional dependence and take these to be in the magnitudes of the hopping amplitudes. The result is summarized in table III.

(a)NNNN: $t_{am;b'_1m'}$				(b)NNNN: $t_{am;b'_2m'}$				(c)NNNN: $t_{am;b'_3m'}$			
$m' \setminus m$	d_{xy}	d_{yz}	d_{zx}	$m' \setminus m$	d_{xy}	d_{yz}	d_{zx}	$m' \setminus m$	d_{xy}	d_{yz}	d_{zx}
d_{xy}	$t_3(b'_1)$	-	-	d_{xy}	-	-	-	d_{xy}	-	-	-
d_{yz}	-	-	-	d_{yz}	-	$t_3(b'_2)$	-	d_{yz}	-	-	-
d_{zx}	-	-	-	d_{zx}	-	-	-	d_{zx}	-	-	$t_3(b'_3)$

TABLE III. The hoppings for the third nearest neighbours

Tight-binding fit to the DFT results indeed show that this hopping energy scale is given by

$$t_3(b'_\alpha) = t_n \approx -0.075$$
 eV (31)

Therefore we have:

$$T_{ab'_\alpha}^{(03)} = \frac{t_n}{3}, \quad T_{ab'_1}^{(z3)} = 0; \tag{32}$$

or,

$$J_{ij}^{(3)} = \frac{4[t_n]^2}{9U}; \quad J_{ij}^{(3z)} = 0; \tag{33}$$

Mean field calculation on the Hamiltonian

We consider the mean field energies of classical Neel and the zig-zag ground states as a function of the different parameters. The classical energy of the Neel state is given by:

$$\frac{E_{Neel}}{S^2 N_{cell} J^{(1)}} = -2 \left(1 + 2 \frac{\tilde{J}_1}{J_1} - 3 \frac{J_2}{J_1} \right) + 6 \left(2 \frac{J_2^z}{J_1} - \frac{J_1^z}{J_1} \right). \quad (34)$$

We define new parameters

$$x = \frac{\tilde{J}_1}{J_1}; \quad y = \frac{J_2}{J_1}; \quad \delta_1 = \frac{J_2^z}{J_1}; \quad \delta_2 = \frac{J_1^z}{J_1}. \quad (35)$$

Here $J_1(\tilde{J}_1)$ is the strong(weak) antiferromagnet exchange between nearest neighbours (see main text for the rest). We get

$$\frac{E_{Neel}}{S^2 N_{cell} J^{(1)}} = -2(1 + 2x - 3y) + 6(2\delta_1 - \delta_2). \quad (36)$$

Similarly, for the Zig-Zag state, we have

$$\frac{E_{Zig-Zag}}{S^2 N_{cell} J^{(1)}} = -2(1 - 2x + 5y) - 2(2\delta_2 - \delta_1) \quad (37)$$

The Zig-Zag state is stable when

$$-x + 2y + (2\delta_2 - \delta_1) > 0 \quad (38)$$

Using Eq. 5 we write the above condition as:

$$-x_0 + 2y_0 + \frac{1}{2}(2\delta_2 - \delta_1) > 0 \quad (39)$$

where, $x_0 = \frac{\tilde{J}^{(01)}}{J^{(01)}}$ and $y_0 = \frac{J^{(02)}}{J^{(01)}}$. We take the Ising anisotropies to be about 5% of the strongest coupling, *i.e.*, $\delta_1 \approx \delta_2 = 0.05$. Thus the Zig-Zag state is stable in the regime

$$y_0 > \frac{1}{2}(x_0 - 0.025). \quad (40)$$

Outside this regime the 2-sublattice Neel state is more stable. This is plotted in Fig. 2.

Spin Wave Spectrum

To calculate the spin wave spectrum for the zig-zag state we use the usual Holstein-Primakoff method suited to collinear ordering which may alternate in direction. More precisely we introduce:

$$S^z = S - a^\dagger a; \quad S^+ = \sqrt{2S}a; \quad S^- = \sqrt{2S}a^\dagger \quad (41)$$

for one direction and

$$S^z = -S + a^\dagger a; \quad S^+ = \sqrt{2S}a^\dagger; \quad S^- = \sqrt{2S}a \quad (42)$$

for the other direction. Since there are 4 sites per unit cell (refer Fig. 1(a)) the quadratic Hamiltonian is a 8×8 matrix given by:

$$H_Q = H_{cl} + H_{sp}, \quad (43)$$

where H_{cl} is the classical part dealt in the previous section. The spin wave Hamiltonian has the following form

$$H_{sp} = \frac{S}{2} \sum_{\mathbf{k}} \Psi_{\mathbf{k}}^\dagger \mathcal{H}_{\mathbf{k}} \Psi_{\mathbf{k}} + H_s \quad (44)$$

Here $\Psi_{\mathbf{k}}^\dagger = [a_{\mathbf{k},1}^\dagger, a_{\mathbf{k},2}^\dagger, a_{\mathbf{k},3}^\dagger, a_{\mathbf{k},4}^\dagger, a_{-\mathbf{k},1}, a_{-\mathbf{k},2}, a_{-\mathbf{k},3}, a_{-\mathbf{k},4}]$ (the subscript 1, 2, 3, 4 refers to the four sites in the unit cell as shown in Fig 1(a)) and

$$H_s = -\frac{S}{2} [(1 - 2x + 5y) - (2\delta_2 - \delta_1)] N_{Cell}; \quad \mathcal{H}_{\mathbf{k}} = \begin{bmatrix} A_{\mathbf{k}} & B_{\mathbf{k}} \\ B_{\mathbf{k}}^\dagger & A_{\mathbf{k}} \end{bmatrix} \quad (45)$$

where N_{cell} is the number of unit cells and

$$A_{\mathbf{k}} = \begin{bmatrix} \chi_{\mathbf{k}} & 0 & 0 & \eta_{\mathbf{k}} \\ 0 & \chi_{\mathbf{k}} & \phi_{\mathbf{k}} & 0 \\ 0 & \phi_{\mathbf{k}}^* & \chi_{\mathbf{k}} & 0 \\ \eta_{\mathbf{k}}^* & 0 & 0 & \chi_{\mathbf{k}} \end{bmatrix}; \quad B_{\mathbf{k}} = \begin{bmatrix} 0 & \xi_{\mathbf{k}} & \rho_{\mathbf{k}} & 0 \\ \xi_{\mathbf{k}}^* & 0 & 0 & \rho_{\mathbf{k}} \\ \rho_{\mathbf{k}}^* & 0 & 0 & \xi_{\mathbf{k}} \\ 0 & \rho_{\mathbf{k}}^* & \xi_{\mathbf{k}} & 0 \end{bmatrix} \quad (46)$$

where,

$$\chi_{\mathbf{k}} = (2\delta_2 - \delta_1) + (1 - 2x + 5y + y \cos k_x); \quad (47)$$

$$\eta_{\mathbf{k}} = x e^{ik_y} (1 + e^{ik_x}); \quad (48)$$

$$\phi_{\mathbf{k}} = x (1 + e^{ik_x}); \quad (49)$$

$$\xi_{\mathbf{k}} = (1 + 2y \cos k_x + y e^{-ik_y}); \quad (50)$$

$$\rho_{\mathbf{k}} = y(1 + e^{ik_x})(1 + e^{-ik_y}). \quad (51)$$

Now following usual methods we diagonalize

$$\begin{bmatrix} A_{\mathbf{k}} & B_{\mathbf{k}} \\ -B_{\mathbf{k}}^\dagger & -A_{\mathbf{k}} \end{bmatrix} \quad (52)$$

to get the spin wave spectrum as plotted in Fig. 3(a) and 3(b).